IMAGE RECONSTRUCTION WITH ACOUSTIC MEASUREMENT USING DISTORTED BORN ITERATION METHOD

C. Lu[1], J. Lin[1], W. Chew[1] and G. Otto[2]

[1] Department of Electrical and Computer Engineering
University of Illinois at Urbana-Champaign
Urbana, IL 61801

[2] ThermoTrex Corporation
9550 Distribution Avenue
San Diego, CA 92121

The distorted Born iterative method (DBIM) is applied to solve electromagnetics and ultrasonics inverse scattering problems. First, we use the DBIM to process the data, which are the scattered fields from two-dimensional cylinders with arbitrary cross section. From this simulation, we confirmed that the first-order Born approximation can be applied to larger objects as long as the phase change of a wave passing through the object due to its presence is smaller than a limit. Then we applied DBIM to process the ultrasonic measurement data. Images for a balloon and an egg that are immersed in water have been reconstructed and compared with those from the first-order diffraction tomography (DT).

Key words: ultrasound imaging; Born iteration; diffraction tomography.

I. INTRODUCTION

Ultrasonic imaging has been widely used in medical applications because it can provide spatial acoustic velocity variations, absorption and scattering properties of objects, and it is relatively safe compared to traditional radiography and X-ray computed tomography. There are a number of methods to reconstruct the ultrasonic images such as pulse-echo imaging, Doppler imaging, sonoelasticity imaging, and computed tomography. A detailed discussion about recent development in ultrasonic imaging techniques can be found in [1-3]. However, in practical applications, one of the main difficulties in this technology is to perform quantitative tissue characterization [1].

Applications of ultrasonic computed diffraction tomography demonstrated potential for tissue characterization [4]. This technique is based on the first-order Born or Rytov approximation [5] and it is computationally efficient due to the fact that, under these approximations, the unknown object function is linearly related to the measured fields by a Fourier transform. Hence, the fast Fourier transform (FFT) can be used to convert the measured fields into an object function—the image. However, both the Born and Rytov approximations are good for weak scatterers only, i.e., the applications are limited to a small range of tissue parameter variations. Slaney *et al* performed extensive studies on the limitations of the first-order Born and Rytov approximations [6] and showed that the first-order Born approximation is valid only for objects for which the product of the relative refractive index and cylinder diameter is less than $0.35\lambda_0$. The first-order Rytov approximation is valid with essentially no constraint on the size of the cylinder; however, the change of refractive index must be less than a few percent. The limitations of the Born approximation is due to multiple scattering effects of objects with high contrast in the the dielectric permittivity. As a result, imaging methods with higher-order approximations (or nonlinear inverse methods) have been investigated and developed [7-14]. The distorted Born iterative method (DBIM) is one of the higher-order approximations, Recently, we implemented the distorted Born iterative method and performed numerical simulations [11]. The algorithm was initially designed for imaging reconstruction with electromagnetic measurements. However, it can also be applied to process ultrasonic data. In this case, the object function is the parameter s which is defined such that $s^2 = k^2 - k_0^2 - \sqrt{\rho}\nabla^2\left(1/\sqrt{\rho}\right)$, where k is the complex wave number, and ρ is the relative density [18]. In this paper, we will show several processing results with this method using simulated data as well as measurement data.

It must be pointed out that higher-order solutions will generally be computationally intensive. Hence, with current computer resources, it is not efficient for interactive diagnosis application, especially in cases of imaging large objects.

The outline of this paper is as follows: We begin with a brief formulation of the method, followed by a description of the measurement set-up. For the numerical reconstructions, we first give some examples to compare the performance of first-order diffraction tomography and the distorted Born approximation. These results can be considered as extensions to those in [6]. We then give the reconstructions using ultrasonic measurement data, and the reconstructions are compared with those obtained by applying diffraction tomography to the same measurement.

II. FORMULATION

Electromagnetic waves and ultrasonic waves satisfy the same partial differential equation in the linear regime. Therefore, in principle, inverse algorithms developed for electromagnetic waves can be used to process ultrasonic data. If nonmagnetic material is assumed, for instance, the 2D electromagnetic scattering problem for the E_z polarization is mapped into the acoustic wave equation for the variable velocity. On the other hand, the 2D electromagnetic scattering problem for the H_z polarization is mapped into the acoustic wave equation for the variable density.

Electromagnetic inverse scattering problems have been intensely studied for many years [10-12,14-16]. There exist in the literature a number of nonlinear electromagnetic inverse algorithms that account for the multiple scattering within the scatterer. The multiple scattering effect makes the inverse problem nonlinear. We will demonstrate the inversion of some ultrasonic data using electromagnetic inverse algorithms we have developed. We will compare the inverted images with linear inversion algorithms such as the diffraction tomography (DT).

These inverse algorithms are driven by a forward solver. We use the conjugate gradient method (CG) to solve the forward scattering problem, in which the fast Fourier transform (FFT) is used to speed up the matrix-vector multiplication [22].

We restrict our discussion to two-dimensions, and assume the time dependency of $e^{-i\omega t}$. The acoustic pressure ϕ satisfies the following partial differential equation [18],

$$\nabla^2\phi(\mathbf{r}) + k_b^2\phi(\mathbf{r}) = -S(\mathbf{r})\phi(\mathbf{r}), \tag{1}$$

where

$$S(\mathbf{r}) = k^2(\mathbf{r}) - k_b^2 - \rho(\mathbf{r})^{1/2}\nabla^2\rho(\mathbf{r})^{-1/2}, \tag{2}$$

$$k(\mathbf{r}) = \frac{\omega}{c(\mathbf{r})} + i\alpha(\mathbf{r}). \tag{3}$$

is the wave number, $c(\mathbf{r})$ is the sound speed, $\alpha(\mathbf{r})$ is the attenuation coefficient, $\rho(\mathbf{r})$ is the density, and $\omega = 2\pi f$ is the angular frequency.

Assuming that the incident wave (pressure) is $\phi^{inc}(\mathbf{r})$, the scattered wave can then be expressed by an integral expression,

$$\phi^{sca}(\mathbf{r}) = \int_S d\mathbf{r}' g_0(k_b, \mathbf{r} - \mathbf{r}') S(\mathbf{r}') \phi(\mathbf{r}'), \tag{4}$$

where $\phi(\mathbf{r}) = \phi^{inc}(\mathbf{r}) + \phi^{sca}(\mathbf{r})$ is the total field inside the inhomogeneous region S and $g_0(k_b, \mathbf{r} - \mathbf{r}')$ is the Green's function for the background. When the background is homogeneous, g_0 in the two-dimensional case is the zeroth-order Hankel function of the first kind,

$$g_0(k_b, \mathbf{r} - \mathbf{r}') = \frac{i}{4} H_0^{(1)}(k_b|\mathbf{r} - \mathbf{r}'|).$$

Eq. (4) may also be written as

$$\phi(\mathbf{r}) = \phi^{inc}(\mathbf{r}) + \int_S d\mathbf{r}' g_0(k_b, \mathbf{r} - \mathbf{r}') S(\mathbf{r}') \phi(\mathbf{r}'). \tag{5}$$

Eq. (5) is a linear equation for the total field $\phi(\mathbf{r})$, and is a nonlinear integral equation of the object function $S(\mathbf{r})$. Solving for the total field $\phi(\mathbf{r})$ with known $S(\mathbf{r})$ is a forward scattering problem. On the other hand, solving for $S(\mathbf{r})$ with the known scattered field (outside the scatterer) is an inverse problem. The forward scattering problem may be solved iteratively using the conjugate gradient method. The forward scattering solution algorithm can be found in several published literatures [12,21]. Here we will focus our discussion on the inverse scattering problem.

A simple solution is to use the first-order Born approximation, which assumes that the total field in the object is equal to the incident field [5]. This is equivalent to the approximation that the scattered field in the object is much smaller than the incident field. Under this assumption, the scattered field can be related to the object function $S(\mathbf{r})$ by a linear relation:

$$\phi^{sca}(\mathbf{r}) = \int_S d\mathbf{r}' \, g_0(k_b, \mathbf{r} - \mathbf{r}') S(\mathbf{r}') \phi^{inc}(\mathbf{r}'). \tag{6}$$

For the measurement where the transmitters and receivers are in the far-field region of the object, we can show that the scattered field can be written as a Fourier transform of the object function [19]. For the near-field measurement case, we can also show that the object function $S(\mathbf{r})$ can be computed using Fourier transforms [18]. Hence, the imaging method under the first-order Born approximation is computationally efficient as the fast Fourier transform (FFT) can be used. (This assumes that the measurement data is dense enough so that interpolation is possible. For measurements where the data is not complete, see [15]).

However, this approximation is valid for weak scatterers only. A scatterer is said to be a weak scatterer if the quantity $k_b \epsilon_r L$ is much smaller than 1 [19], in which L is the size of the object. In [6], Slaney *et al* performed extensive studies of the first-order Born approximation for the inverse scattering of the two-dimensional dielectric cylinder, and gave criteria for the validity of the first-order Born approximation. In the numerical result of this paper, we have simulated cases for the noncircular object, and confirmed the conclusion for the first-order Born approximation given in [6].

There are at least two reasons to apply higher-order approximations to the inverse scattering problem. First of all, in cases that we have no *a priori* knowledge of the contrast and/or size of the object, higher-order solutions can be used to test the validity of the reconstruction with the first-order Born approximation. Secondly, in cases where the object size is large, higher-order methods are required to perform the reconstruction.

The distorted Born iterative method (DBIM) is one of the higher-order nonlinear inversion methods to solve the inverse scattering problems. The basic steps in DBIM are given below. For a more detailed discussion on DBIM, please refer to [10,11].

We first discuss the Born iterative method. It is noted that there are two unknown functions in Eq. (5), the total field $\phi(\mathbf{r})$ and object function $S(\mathbf{r})$. The basic idea of the Born iterative method is to alternatively fix one of them, and solve for the other. (For the method that solves for both unknown functions simultaneously, refer to [20]). To begin, the unknown object function $S(\mathbf{r})$ is assumed to be zero. Hence, the total field is equal to the incident field. We then replace the total field in the integrand of Eq. (5) by the incident field, and solve for $S(\mathbf{r}) \simeq S_0(\mathbf{r})$. Apparently, the solution $S_0(\mathbf{r})$ is from the first-order Born approximation. Next, we replace $S(\mathbf{r})$ in the integrand of Eq. (5) by $S_0(\mathbf{r})$, and solve for the total field $\phi(\mathbf{r})$. We then use $\phi(\mathbf{r})$ in Eq. (5) to solve for $S(\mathbf{r}) \simeq S_1(\mathbf{r})$. These steps are repeated until we get a convergent result.

In this process, the Green's function g_0 is used throughout all the iterations. The distorted Born iterative method differs from the above in that the Green's function $g_0(k_b, \mathbf{r}-\mathbf{r}')$ is updated to $g(k_1, \mathbf{r}-\mathbf{r}')$ in the first iteration, and update to $g(k_2, \mathbf{r}-\mathbf{r}')$ in the second iteration, and so on, where k_1 and k_2 correspond to object function S_1 and S_2, respectively.

Note that in the above description of the iteration process, the total field is solved in each iteration using the last reconstructed object function. Physically, this solution of the total field can be interpreted as the field due to a transmitter (a line source, in this case) in the presence of the current media (which is characterized by the last reconstructed object function). This value is nothing but that of the Green's function for the background media in the presence of the object with parameters of the last reconstruction. Hence, this value is saved and used as the Green's function of the next reconstruction. Reference [10] contains more details on the updating of the Green's function.

Diffraction tomography uses the Born approximation to compute the object function $S(\mathbf{r})$. The resulting algorithm is very efficient since FFT can be applied. The higher-order methods, on the other hand, are more costly. As a result, fast algorithms have been developed [12]. It has been shown that algorithms with computational complexity of $O(N^{1.5}\log N)$ per iteration are possible by applying the CGFFT in the forward scattering solution [12,21].

In the following sections, we will demonstrate the use of DBIM to process the experiment and synthetic data.

III. MEASUREMENT

The data are acquired from a Sonic CT device at ThermoTrex Corp., San Diego, CA. Here we will give a brief description to the experimental set-up. Only the parameters that are related to our numerical simulation are given. For detailed information regarding the experiment, readers may refer to [18]. The device consists of 512 transducers that are uniformly distributed on the circular boundary of a tank (Fig. 1). The tank is of radius $R_0 = 21.08$ cm and filled with fresh water, with velocity $v_w = 1500$ m/s. The target to be measured is hung by a thin wire (60 microns in diameter) and put into the water. Each transducer may act both as a transmitter and as a receiver. With this set-up, 512×512 data points are acquired for three frequencies.

The transducers radiate as dipoles with the peak always pointing toward the origin. The radiation field of a transducer can be calculated using the following formula:

$$\phi^{inc}(\mathbf{r}_R) = -\frac{i}{4}\hat{r}_1 \cdot \hat{r}_T H_1^{(1)}(kr_1), \tag{7}$$

where $\mathbf{r}_1 = \mathbf{r}_R - \mathbf{r}_T$, $\mathbf{r}_R$ is the receiver location, and $\mathbf{r}_T$ is the transmitter location. To obtain the scattered field, the total field is measured first. Then the measured field is multiplied by a calibration constant. Finally, the scattered field is obtained by subtracting the incident field from the total field. Here, the incident field is calculated using Eq. (7).

Since the radiation (receiving) pattern of the transducers are modeled by dipoles, the measured data are for configuration of dipole transmitters and dipole receivers. The currently-implemented DBIM algorithm requires that both transmitters and receivers be monopoles. Appendix A gives the equations to perform the data transformation. This configuration transformation is solely designed to meet the code requirement for the experimental data. (We are aware that a direct reconstruction using the dipole-dipole measurement is possible. However, this is beyond the scope of this paper).

IV. NUMERICAL RESULTS

As mentioned in the previous sections, the first-order Born approximation is valid for weak scatterers only. In this section, we first give numerical examples to evaluate the results of the first-order Born approximation by comparing the images reconstructed by the diffraction tomography (DT) and the distorted Born iterative method (DBIM) for the electromagnetic case. The objects used in this simulation are two-dimensional dielectric cylinders with arbitrary cross section. The first object is shown in figure 2. The dark region corresponds to dielectric permittivity $\epsilon_r > 1$, and the white region corresponds to background with $\epsilon_r = 1$ (the size of the reconstruction region is a square of side length 3.84 m). Thirty-two transmitters and thirty-two receivers are equally placed on a circle of radius 8.0 m. The operating frequency is 300 MHz.

Figures 3 and 4 are the comparisons of the images reconstructed by DT and DBIM for the cases with $\epsilon_r = 1.1$ and 1.5, respectively. It can be seen that the differences are small between the images of the two methods. One explanation is that the multiple scattering has a small effect on the phase of the field for such a thin object. When we increase the volume of the scatterers, we can see the differences [6], as shown in figures 5 and 6. (In these figures, the true object is a cylinder of square cross section with side length 1.6 m. The numbers of the receivers and the transmitters used in the simulation are 32). There are two reasons for the assurance of the independence of the simulation: (a) the reconstruction made using the experimental set-up parameters and the measured data only, and without any *a priori* knowledge of the contrast and the size of the object. (b) There are a number of ways to solve a forward scattering problem. For example, one can use the harmonic expansion method to solve the scattering problem from a circular cylinder, but use the method of moments as the forward solver in the reconstruction algorithms. The above examples showed that the first-order Born approximation will give satisfactory imaging as long as the total phase change caused by the object is less than π as given in [6]. Here, the phase change is the average value of $k_b \int (\epsilon_r - 1)\, dl$, where the integral path is over a straight line through the object.

Next, we apply DBIM to process the ultrasonic measurement data provided by Thermotrex Corp. The first set of the data is the measurement for a balloon immersed in water. The frequency is 312.5 kHz, which corresponds to a wavelength of 4.8 mm in water. The numbers of transmitters and receivers are both 128, and the reconstruction region is a square with 128×128 grid points (the grid size is 0.6 mm). The reconstructed images are shown in figure 7 (note that shown in the figure is a part of the reconstruction region). The reconstruction with data measured for an egg is shown in figure 8. In this case, the frequency is 468.75 kHz, the numbers of receivers and transmitters are both 256. The reconstruction region is a square with 180×180 grid points (the grid size is 0.368 mm). As a comparison, the DT results [18] for both the balloon and the egg are also shown in figures 9 and 10. (For the egg case, the DT results are the average over three frequencies 343.75 kHz, 406.25 kHz, and 468.75 kHz). The spots in figures 7 to 10 are due to the supporting wire. Note that there are horizontal flips between figures 7 and 9, and figures 8 and 10. This is due to different ordering directions of the transmitters for the two reconstruction codes. The reconstruction quality needs further verification. At this time, the detailed physical properties of the balloon and the inside material are not available.

V. CONCLUSION

We have conducted numerical simulations using the distorted Born iterative method (DBIM) and the diffraction tomography (DT) based on the first-order Born approximation. The images from the two methods are compared. We also applied both DBIM and DT to process the ultrasonic measurement data. Numerical results showed that DBIM usually gives improved results over DT for cases involving large objects and high permittivity contrasts.

ACKNOWLEDGMENTS

This work was supported by the Office of Naval Research under grant N00014-95-1-0872 and the National Science Foundation under grant NSF ECS 93-02145.

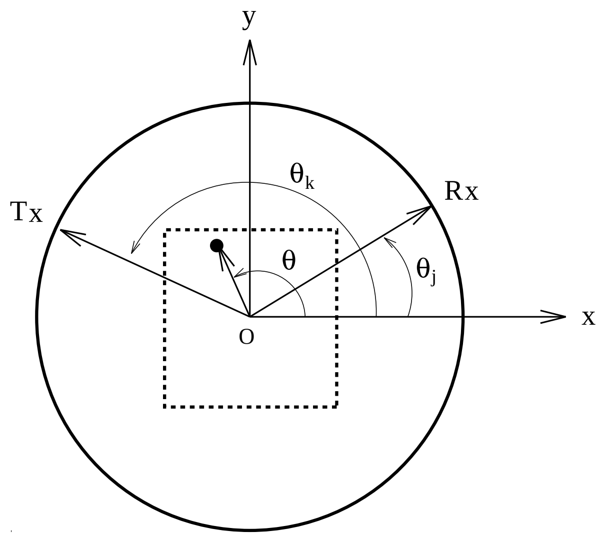

Fig. 1 Measurement set-up. Transmitters T_x and receivers R_x are equally spaced on a circle of radius R_0. The square with the dash line boundary is the reconstruction region which is discretized into cells. Each cell is a small square with size Δ^2, where Δ is much smaller than the wavelength λ_0 (typically $\Delta = 0.1\lambda_0$) and where λ_0 is the wavelength with respect to free space.

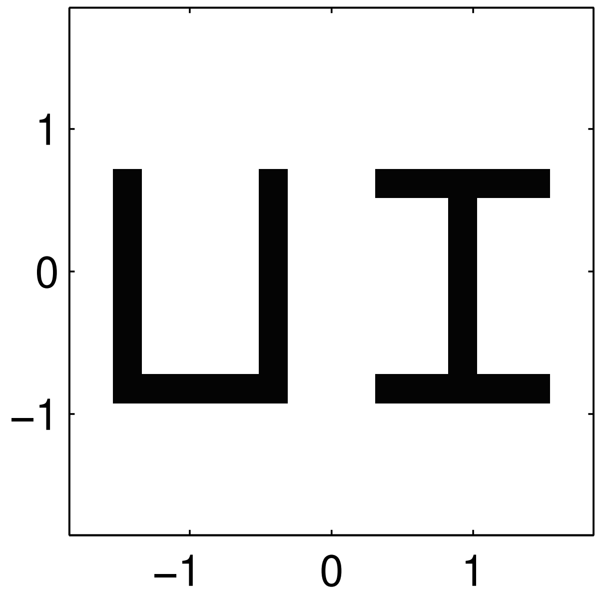

Fig. 2 The true image of ϵ_r of an object used in simulation. The dark region stands for the dielectric material of uniform permittivity ϵ_r, and the white region stands for the homogeneous background with $\epsilon_r = 1$. The coordinate unit is in meters.

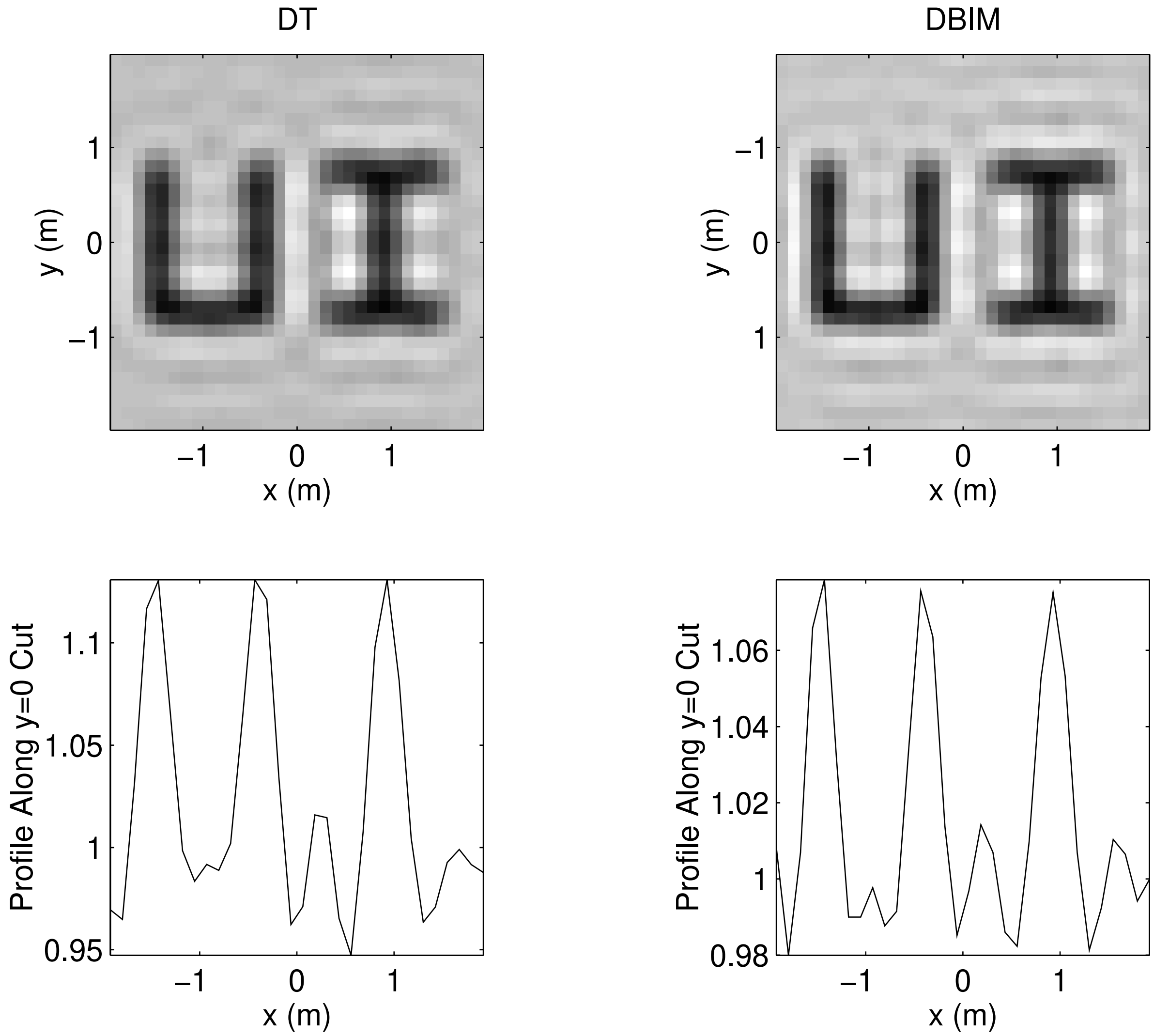

Fig. 3 Comparison of images reconstructed using DBIM and DT for $\epsilon_r = 1.1$ (the true image is shown in figure 2). The reconstruction region consists of 32×32 cells, and each cell is a square of size $0.12\lambda_0 \times 0.12\lambda_0$. In the numerical simulation, 32 transmitters and receivers are used.

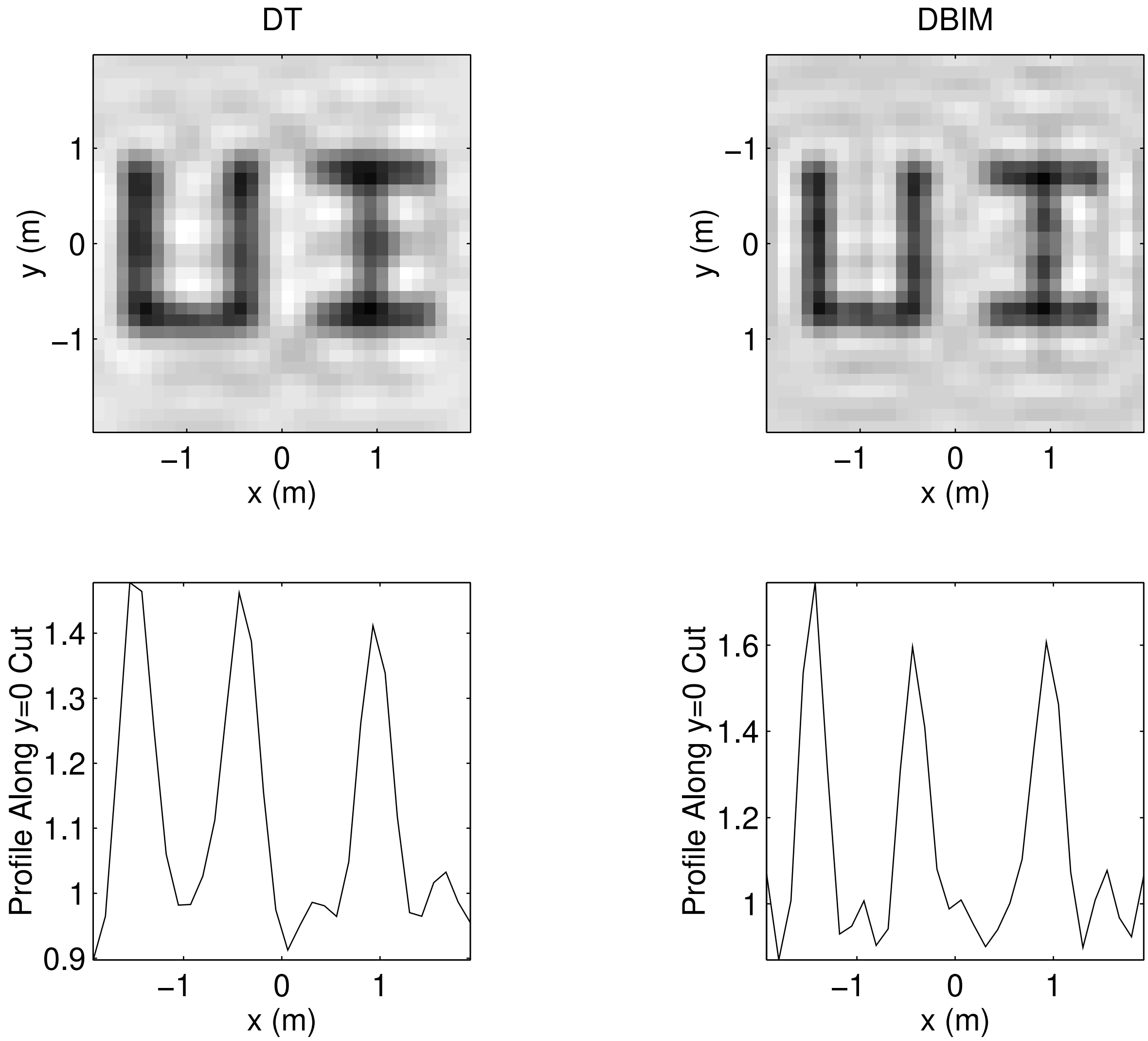

Fig. 4 Same comparison as in figure 3 for $\epsilon_r = 1.5$.

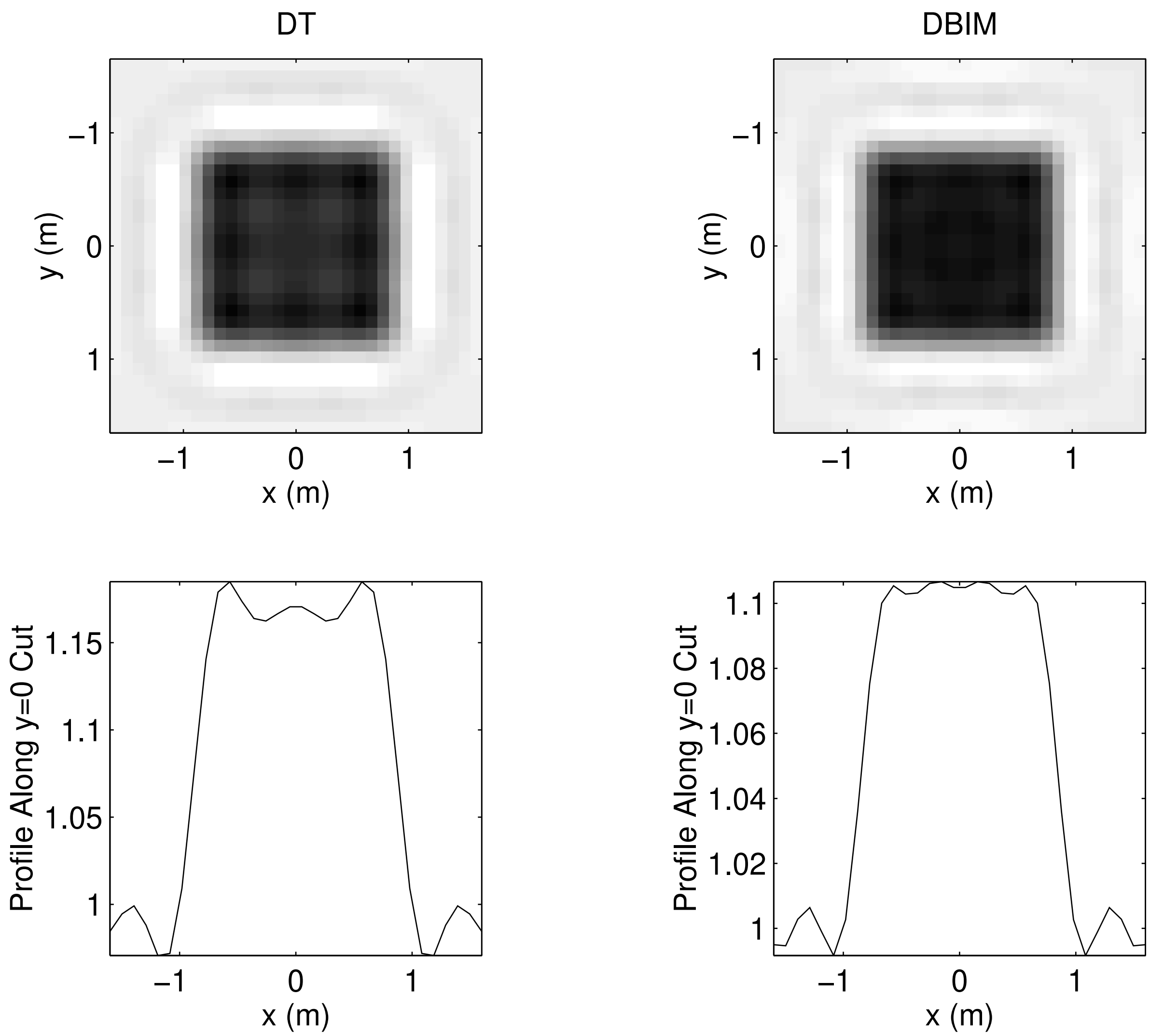

Fig. 5 Comparison of images reconstructed using DBIM and DT for $\epsilon_r = 1.1$. The object is a square cylinder with side length 1.6 λ_0. The reconstruction region consists of 32×32 cells, and each cell is a small square of size $0.1\lambda_0 \times 0.1\lambda_0$. thirty-two transmitters and receivers are used in the simulation.

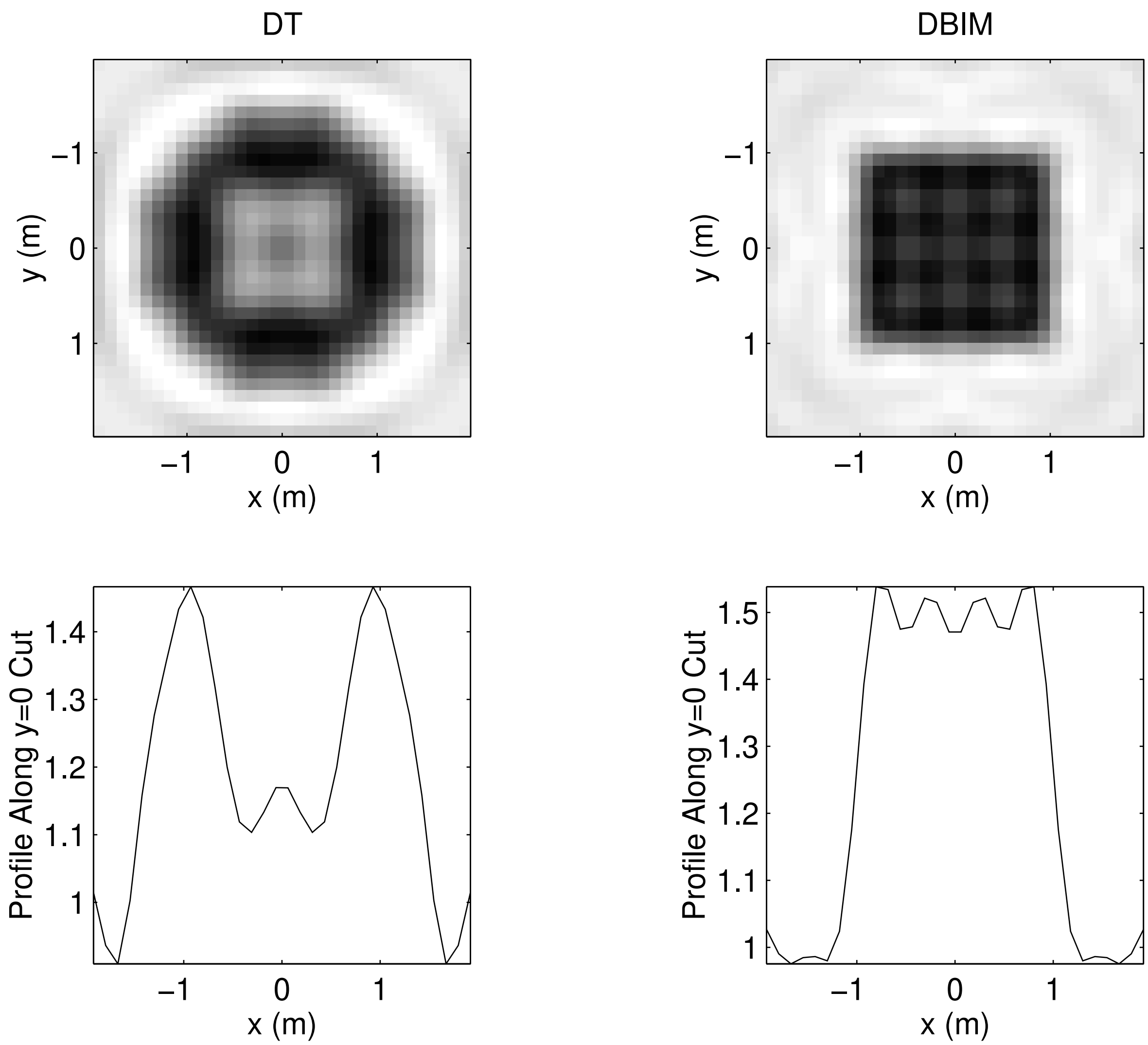

Fig. 6 Same comparison as in figure 5 for $\epsilon_r = 1.5$.

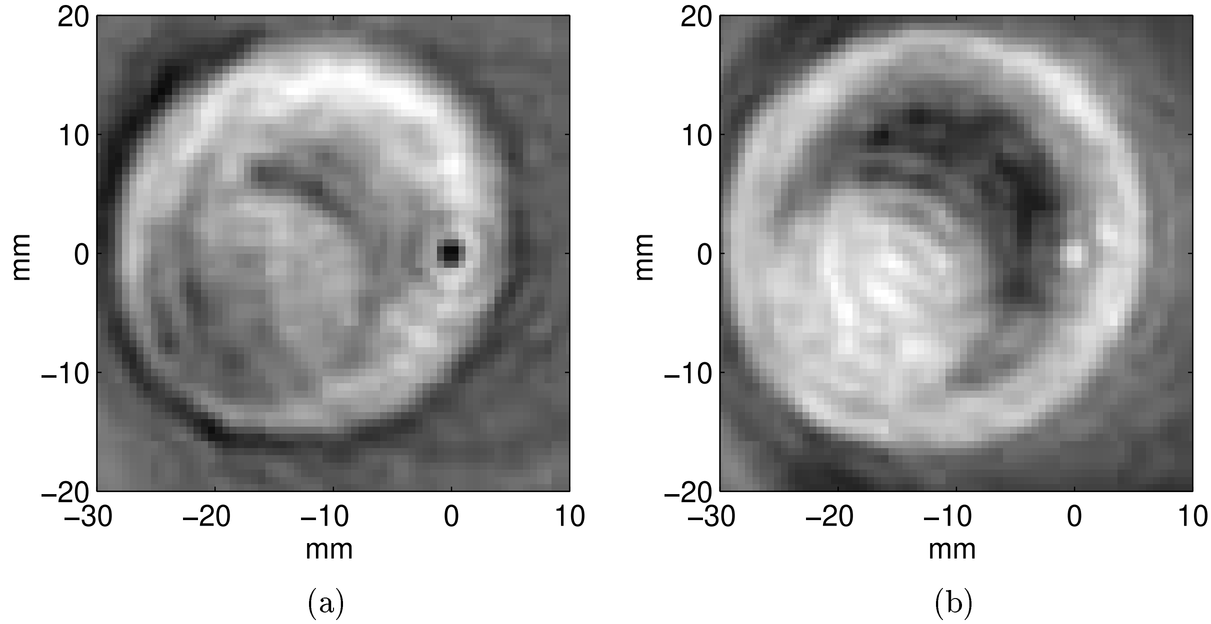

Fig. 7 DBIM reconstruction of a balloon immersed in water: (a) real part, (b) imaginary part.

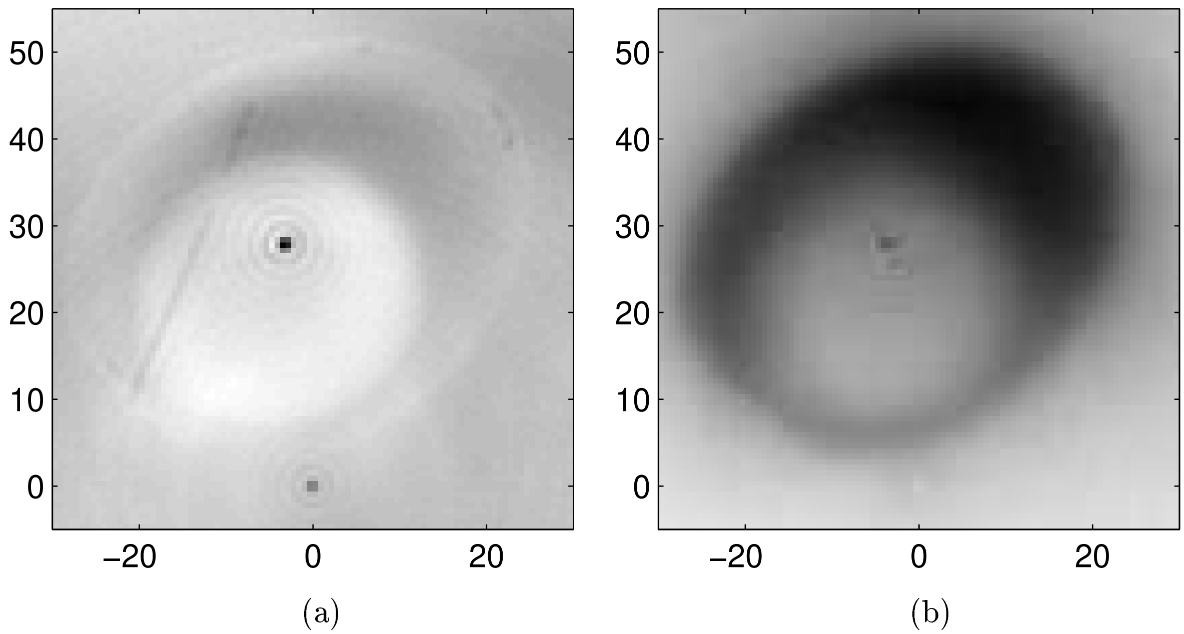

Fig. 8 DBIM reconstruction of a boiled egg immersed in water: (a) real part, (b) imaginary part. The coordinate unit is in mm.

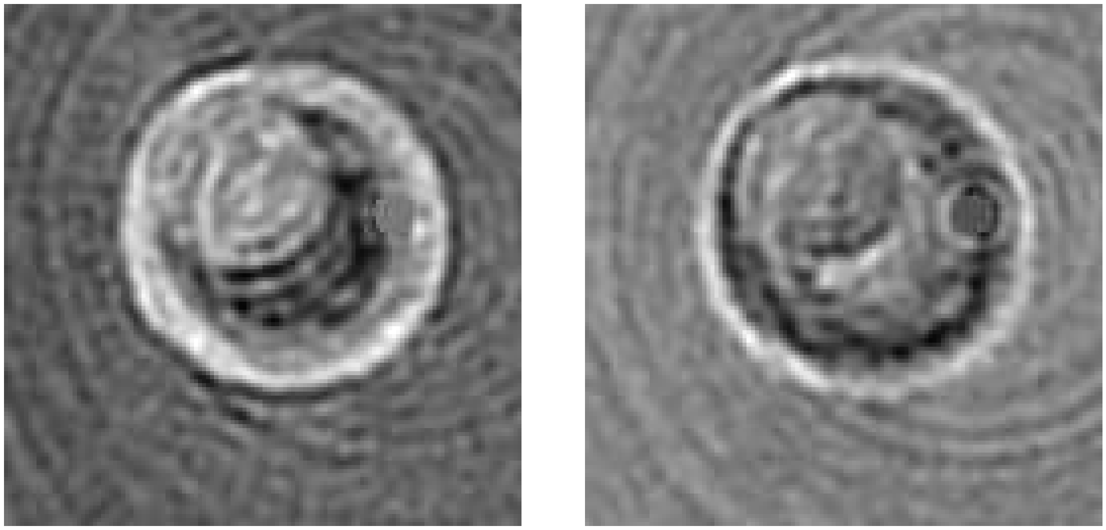

(a) (b)

Fig. 9 DT reconstruction of a balloon immersed in water: (a) real part, (b) imaginary part.

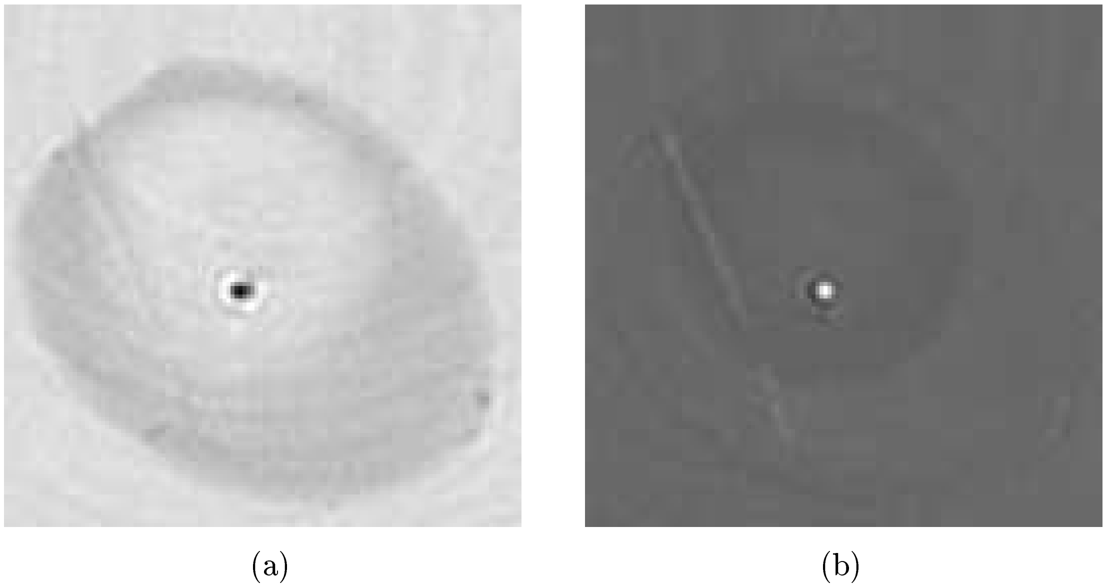

Fig.10 DT reconstruction of a boiled egg immersed in water: (a) real part, (b) imaginary part.

APPENDIX: DATA TRANSFORMATION

The radiation field of a monopole transmitter can be written as

$$\Phi^{(0)}(\mathbf{r}) = H_0^{(1)}(k|\mathbf{r} - \mathbf{r}_s|) \tag{A.1}$$

where, $\mathbf{r}$ is the field position, and $\mathbf{r}_s$ is the source position.

A dipole transmitter can be formed by two monopoles with infinitely large amplitude P in different signs and infinitely small distance δ such that $P\delta$ is a constant. With this definition, the radiation pattern of a dipole with maximum radiation in $\hat{r}_s$ direction can be written as

$$\Phi^{(1)}(\mathbf{r}) = PH_0^{(1)}(k|\mathbf{r} - (\mathbf{r}_s + \delta\hat{r}_s)|) - PH_0^{(1)}(k|\mathbf{r} - (\mathbf{r}_s - \delta\hat{r}_s)|).$$

Since $\delta \ll |\mathbf{r} - \mathbf{r}_s|$, we have

$$|\mathbf{r} - (\mathbf{r}_s \mp \delta\hat{r}_s))| \sim r_1 \pm \delta\hat{r}_1 \cdot \hat{r}_s, \qquad \mathbf{r}_1 = \mathbf{r} - \mathbf{r}_s.$$

Using Taylor series, we have

$$\begin{aligned} H_0^{(1)}(k|\mathbf{r} - (\mathbf{r}_s \mp \delta\hat{r}_s)|) =& H_0^{(1)}(kr_1 \pm k\delta\hat{r}_1 \cdot \hat{r}_s) \\ \approx& H_0^{(1)}(kr_1) \pm k\delta\hat{r}_1 \cdot \hat{r}_s H_0^{(1)'}(kr_1). \end{aligned}$$

As a result, $\Phi^{(1)}$ can be written as:

$$\begin{aligned} \Phi^{(1)}(\mathbf{r}) \approx& 2kP\delta\hat{r}_1 \cdot \hat{r}_s H_1^{(1)}(kr_1) \\ =& kP\delta \left[H_1^{(1)}(kr_1)e^{i(\theta_1 - \theta_s)} + H_1^{(1)}(kr_1)e^{-i(\theta_1 - \theta_s)} \right] \end{aligned} \tag{A.2}$$

where $\mathbf{r}_1 = \mathbf{r} - \mathbf{r}_s$, and θ_1 is the polar angle of $\mathbf{r}_1$. The relation $H_0^{(1)'} = -H_1^{(1)}$ has been used.

Applying the addition theorem to $H_{\pm 1}^{(1)}(kr_1)e^{\pm i\theta_1}$:

$$H_{\pm 1}^{(1)}(kr_1)e^{\pm i\theta_1} = \sum_{n=-\infty}^{\infty} H_{n\mp 1}^{(1)}(kr_s)e^{-i(n\mp 1)\theta_s} J_n(kr)e^{in\theta}, \qquad r_s > r.$$

Hence,

$$\begin{aligned} \Phi^{(1)}(\mathbf{r}) =& kP\delta \sum_{n=-\infty}^{\infty} \left(H_{n-1}^{(1)}(kr_s) - H_{n+1}^{(1)}(kr_s) \right) J_n(kr)e^{in(\theta-\theta_s)} \\ =& 2kP\delta \sum_{n=-\infty}^{\infty} H_n'(kr_s)J_n(kr)e^{in(\theta-\theta_s)}. \end{aligned}$$

The dipole received field is the same as the summation of two monopoles separated by 2δ with different signs:

$$\Phi_R^{(1)} = PH_0^{(1)}(k|\mathbf{r} + \delta\hat{r} - \mathbf{r}'|) - PH_0^{(1)}(k|\mathbf{r} - \delta\hat{r} - \mathbf{r}'|).$$

Using a similar manner as in the above section, we can show that

$$\Phi_R^{(1)} = -2Pk\delta\hat{r}_2 \cdot \hat{r} H_1^{(1)}(kr_2),$$

where $\mathbf{r}_2 = \mathbf{r} - \mathbf{r}'$.

The integral equation is

$$E(\mathbf{r}) = E^{inc}(\mathbf{r}) + \frac{i}{4}\int_S dS' H_0^{(1)}(k|\mathbf{r} - \mathbf{r}'|)O(\mathbf{r}')E(\mathbf{r}'), \tag{A.3}$$

where

$$E^{inc}(\mathbf{r}) = \begin{cases} \frac{i}{4}H_0^{(1)}(kr_1), & \text{Monopole excitation,} \\ \frac{i}{4}(2k\delta P\hat{r}_1 \cdot \hat{r}_s)H_1^{(1)}(kr_1), & \text{Dipole excitation,} \end{cases}$$

where $\mathbf{r}_1 = \mathbf{r} - \mathbf{r}_s$.

When the total field $E(\mathbf{r})$ is solved, the field received by the receiver can be calculated by

$$\begin{bmatrix} \Phi^{(0)}(\mathbf{r}_R) \\ \Phi^{(1)}(\mathbf{r}_R) \end{bmatrix} = \frac{i}{4}\int_S dS' \begin{bmatrix} H_0^{(1)}(kr_2) \\ -2k\delta P\hat{r}_2 \cdot \hat{r} H_1^{(1)}(kr_2) \end{bmatrix} O(\mathbf{r}')E(\mathbf{r}'), \tag{A.4}$$

where, $\mathbf{r}_2 = \mathbf{r}_R - \mathbf{r}'$.

The dipole/dipole measured data $m_{jk}^{(1)}$ can be written as

$$m_{jk}^{(1)} = \sum_{p,q=-\infty}^{\infty} \int d\mathbf{x} H_p'(k_0r_0)H_q'(k_0r_0)J_p(k_0r)J_q(k_0r)e^{ip(\theta-\theta_j)+iq(\theta-\theta_k)}S(\mathbf{x}), \tag{A.5}$$

where k_0 is the background wave number, $\mathbf{r}$ is the location in the unknown media, r_0 is the receiver location, $S(\mathbf{x})$ is the unknown media parameter, j and k are the indices for the receivers and transmitters. The geometry of the measurement configuration is shown in figure A.1.

In the same manner, the monopole/monopole measurement $m_{jk}^{(0)}$ can also be written as

$$m_{jk}^{(0)} = \sum_{p,q=-\infty}^{\infty} \int d\mathbf{x} H_p^{(1)}(k_0r_0)H_q^{(1)}(k_0r_0)J_p(k_0r)J_q(k_0r)e^{ip(\theta-\theta_j)+iq(\theta-\theta_k)}S(\mathbf{x}). \tag{A.6}$$

By defining

$$X_{pq} = \int d\mathbf{x} J_p(k_0 r) J_q(k_0 r) e^{i(p+q)\theta} S(\mathbf{x}), \tag{A.7}$$

then, Eqs. (A.5) and (A.6) can be written as

$$m_{jk}^{(1)} = \sum_{p,q=-\infty}^{\infty} X_{pq} H_p^{(1)'}(k_0 r_0) H_q^{(1)'}(k_0 r_0) e^{-ip\theta_j - iq\theta_k} \tag{A.8}$$

and

$$m_{jk}^{(0)} = \sum_{p,q=-\infty}^{\infty} X_{pq} H_p^{(1)}(k_0 r_0) H_q^{(1)}(k_0 r_0) e^{-ip\theta_j - iq\theta_k}. \tag{A.9}$$

Now, it is clear that $m_{jk}^{(1)}$ is the two-dimensional discretized Fourier transform $\mathcal{F}_2$ of $X_{pq} H_p^{(1)'}(k_0 r_0) H_q^{(1)'}(k_0 r_0)$, and $m_{jk}^{(0)}$ is the two-dimensional discretized Fourier transform $\mathcal{F}_2$ of $X_{pq} H_p^{(1)}(k_0 r_0) H_q^{(1)}(k_0 r_0)$. Thus, we have

$$m_{jk}^{(1)} = \mathcal{F}_2 \left[X_{pq} H_p^{(1)'}(k_0 r_0) H_q^{(1)'}(k_0 r_0) \right] \tag{A.10}$$

$$m_{jk}^{(0)} = \mathcal{F}_2 \left[X_{pq} H_p^{(1)}(k_0 r_0) H_q^{(1)}(k_0 r_0) \right]. \tag{A.11}$$

Applying the inverse Fourier transform $\mathcal{F}_2^{-1}$, we have

$$X_{pq} H_p^{(1)'}(k_0 r_0) H_q^{(1)'}(k_0 r_0) = \mathcal{F}_2^{-1}(m_{jk}^{(1)}). \tag{A.12}$$

From the above equation, we find that

$$X_{pq} = \frac{\mathcal{F}_2^{-1}\left(m_{jk}^{(1)}\right)}{H_p^{(1)'}(k_0 r_0) H_q^{(1)'}(k_0 r_0)}. \tag{A.13}$$

Substituting Eqs. (A.13) into (A.9), we obtain

$$m_{jk}^{(0)} = \mathcal{F}_2 \left[\frac{H_p^{(1)}(k_0 r_0) H_q^{(1)}(k_0 r_0)}{H_p^{(1)'}(k_0 r_0) H_q^{(1)'}(k_0 r_0)} \mathcal{F}_2^{-1}\left(m_{jk}^{(1)}\right) \right]. \tag{A.14}$$

Eq. (A.14) describes the relation between the monopole response to monopole transmitters and the dipole response to dipole transmitters. From this equation, we can see that in order to perform the transformation, the distribution of both transmitters and receivers must be dense enough so that DFT is possible.

In Eqs. (A.10) to (A.14), $\mathcal{F}_2$ is a symbol referring to the two-dimensional discretized Fourier transform. For the numerical calculation, the infinite series in the transformation must be truncated. We define the truncated version of $\mathcal{F}_2$ as

$$\tilde{X}_{jk} = \mathrm{DFT}\left[X_{qp}\right]_{jk} = \sum_{p,q=0}^{N-1} X_{pq} e^{-i\frac{2\pi}{N}(jp+kq)} \tag{A.15}$$

$$X_{pq} = \frac{1}{N^2}\mathrm{IDFT}\left[\tilde{X}_{jk}\right]_{pq} = \frac{1}{N^2}\sum_{j,k=0}^{N-1} \tilde{X}_{jk} e^{i\frac{2\pi}{N}(pj+qk)}. \tag{A.16}$$

Truncating the summation over p and q in Eq. (A.5) at M ($2M < N$), padding zeros for X_{pq} from $2M+1$ to $N-1$, and assuming that θ_j and θ_k are uniformly distributed on the r_0 circle, i.e.,

$$\theta_j = \frac{2\pi}{N}j, \quad \theta_k = \frac{2\pi}{N}k, \qquad j,k = 0,1,\cdots,N-1, \tag{A.17}$$

then, we have:

$$m_{jk}^{(1)} = e^{i\frac{2\pi M}{N}(j+k)} \sum_{p,q=0}^{2M} X_{p-M,q-M} H_{p-M}^{(1)'}(k_0 r_0) H_{q-M}^{(1)'}(k_0 r_0) e^{-i\frac{2\pi}{N}(jp+kq)} \tag{A.18}$$

$$X_{p-M,q-M} H_{p-M}^{(1)'}(k_0 r_0) H_{q-M}^{(1)'}(k_0 r_0) = \frac{1}{N^2}\mathrm{IDFT}\left[m_{jk}^{(1)} e^{-i\frac{2\pi M}{N}(j+k)}\right], \tag{A.19}$$

and

$$m_{jk}^{(0)} = \frac{e^{i\frac{2\pi M}{N}(j+k)}}{N^2}\mathrm{DFT}\left[\frac{H_{p-M}^{(1)} H_{q-M}^{(1)}}{A.H_{p-M}^{(1)'} H_{p-M}^{(1)'}}\mathrm{IDFT}\left[m_{jk}^{(1)} e^{-i\frac{2\pi M}{N}(j+k)}\right]_{pq}\right]_{jk}. \tag{A.20}$$

The test procedures are given below:

(1) Assume $\mathbf{r}_i$, $i = 1,2,\cdots,N$ are uniformly distributed on a circle that encloses the scatterer. Let $2k\delta P = 1$.

(2) Solve Eq. (A.3) for $E(\mathbf{r})$ with monopole and dipole excitations, respectively, for $\mathbf{r}_s = \mathbf{r}_i$, $i = 1,2,\cdots,N$.

(3) Calculate $\overline{\boldsymbol{\Phi}}^{(0)}(\mathbf{r}_R)$ and $\overline{\boldsymbol{\Phi}}^{(1)}(\mathbf{r}_R)$ using Eq. (A.4), for $\mathbf{r}_R = \mathbf{r}_i$, $i = 1,2,\cdots,N$.

(4) Let $\overline{\mathbf{m}}^{(1)} = \overline{\boldsymbol{\Phi}}^{(1)}(\mathbf{r}_R)$, calculate $\overline{\mathbf{m}}^{(0)}$ using Eq. (A.20).

(5) Compare $\overline{\mathbf{m}}^{(0)}$ with $\overline{\boldsymbol{\Phi}}^{(0)}(\mathbf{r}_R)$.

Figure A.2 shows a numerical simulation. In this simulation, the scatterer is a rectangular dielectric scatterer with $\epsilon_r = 2.5 + i0.5$ and $\mu_r = 1$. The size of the scatterer is $1\lambda_0 \times 1\lambda_0$, where $\lambda_0 = 1$ m. Thirty-two transmitters and 32 receivers are uniformly distributed on the circle of radius $R = 5m$. The scatterer is divided into 100 subscatterers and the forward problem is solved by the conjugate gradient method (CG). One can see that the agreement is excellent.

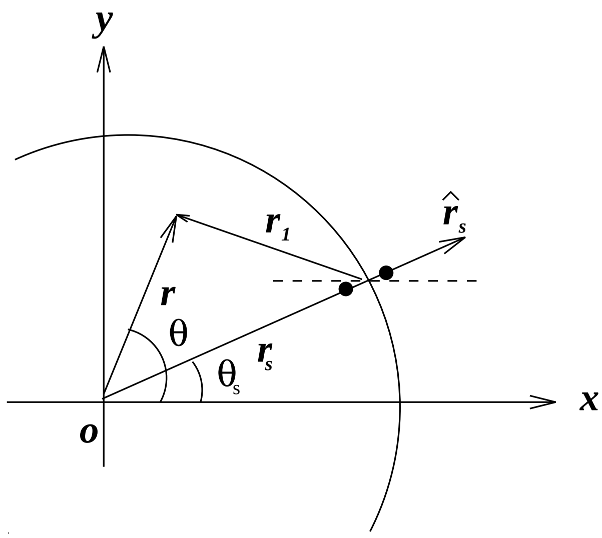

Fig. A.1 The coordinate relation for the addition theorem.

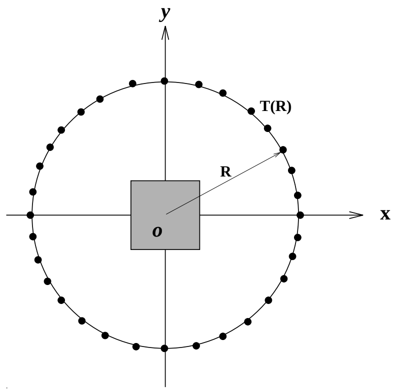

(a)

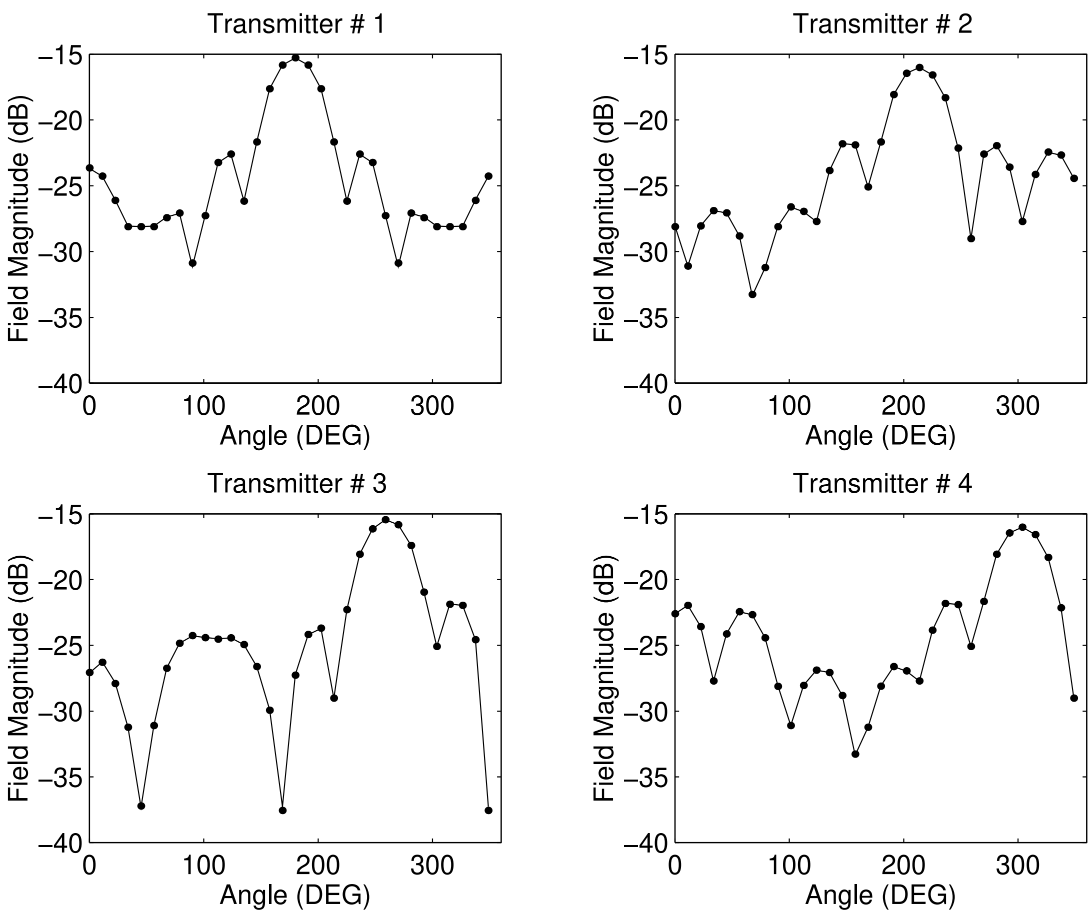

(b)

Fig. A.2 (a). Configuration. (b). Simulation result. Solid line: Direct forward solver. Solid circle: Transformed from dipole/dipole calculation.

REFERENCES

[1] Wells, P. N. T., The present status of ultrasonic imaging in medicine, *Ultrasonics 31*, 345-352 (1993).

[2] Jones, W., Recent activity in ultrasonic tomography, *Ultrasonics 31*, 353-360 (1993).

[3] Kak, A. C., Computerized tomography with X-rays, emission, and ultrasound sources, *IEEE Proc. 67*, 1245-1272 (1979).

[4] Hiller, D., and Ermert, H., Ultrasound computerized tomography using transmission and reflection mode: application to medical diagnosis, in *Acoustical Imaging,* vol.12, pp. 553-564 (Edited by Eric A. Ash and C. R. Hill, Plenum Press, New York, July 19, 1982).

[5] Born, M., and Wolf, E., *Principles of Optics*, 6th Ed., (Pergamon Press, New York, 1980).

[6] Slaney, M., Kak, A. C., and Larsen, L., Limitations of Imaging with First-order Diffraction Tomography, *IEEE Trans. Microwave Theory Tech. 32*, 860-874 (1984).

[7] Cavicchi, T. J. and O'Brien Jr., W. D., Numerical study of higher-order diffraction tomography via the sinc basis moment method, *Ultrasonic Imaging 11*, 42-74 (1989).

[8] Colton, D., and Monk, P., The detection and monitoring of leukemia using electromagnetic waves, *Inverse Problems 11*, 329-342 (1995).

[9] Colton, D., and Monk, P., A modified dual space method for solving the electromagnetic inverse scattering problem for an infinite cylinder, *Inverse Problems 10*, 87-107 (1994).

[10] Wang, Y. M., *Theory and Applications of Scattering and Inverse Scattering Problems*, Ph.D. Thesis (University of Illinois at Urbana-Champaign, 1991).

[11] Wang, Y. M., and Chew, W. C., Accelerating the inverse scattering algorithms by using the fast recursive aggregate T-matrix algorithm," *Radio Science 27*, 109-116 (1992).

[12] Lin, J. H., *A study of iterative methods on forward and inverse scattering problems*, Ph.D. thesis (University of Illinois at Urbana-Champaign, 1995).

[13] Ghodgonkar, D. K., Gandhi, O. P., and Hagmann, M. J., Estimation of complex permittivities of three dimensional inhomogeneous biological bodies, *IEEE Trans. Microwave Theory Tech. 31*, 442-446 (1983).

[14] Bolomey, J. Ch., Durix, Ch., and Lesselier, D., Determination of donductivity profiles by time-domain reflectometry, *IEEE Trans. Antennas and Prop. 27*, 244-248 (1979).

[15] Devaney, A. J., Geophysical diffraction tomography, *IEEE Trans. Geoscience Remote Sensing 22*, 3-13 (1984).

[16] Johnson, S. J., and Tracy, M. L., Inverse scattering solutions by a sinc basis, multiple source, moment method - Part I: Theory, *Ultrasonic Imaging 5*, 361-375 (1983).

[17] Johnson, S. J., and Tracy, M. L., Inverse scattering solutions by a sinc basis, multiple source, moment method - Part II: Numerical evaluations, *Ultrasonic Imaging 5*, 376-392 (1983).

[18] Michael, P. A., Martin, P. J., Otto, G. P., Olson, L. K., Barrett, T. K., Spivey, B. A., and Palmer, D. A., A new consideration of diffraction computed tomography for breast imaging: studies in phantoms and patients, *Acoustic Imaging 21*, 379-390 (1995).

[19] Chew, W. C., *Waves and Fields in Inhomogeneous Media* (Van Nostrand Reinhold, New York, 1990).

[20] Kleinman, R. E., and van den Berg, P. M., A Modified gradient method for two dimensional problems in tomography, *J. Comput. Appl. Math. 42*, 17-35 (1992).

[21] Borup, D. T., Johnson, S. A., Kim, W. W., and Berggren, M. J., Nonperturbative diffraction tomography via Gauss-Newton iterative applied to the scattering integral equation, *Ultrasonic Imaging 14*, 69-85 (1992).